JPL Publication 11-1

HyspIRI Level-2 TIR Surface Radiance Algorithm Theoretical Basis Document

G. Hulley
S. Hook
Jet Propulsion Laboratory

National Aeronautics and Space Administration

Jet Propulsion Laboratory
California Institute of Technology
Pasadena, California

April 2011

This research was carried out at the Jet Propulsion Laboratory, California Institute of Technology, under a contract with the National Aeronautics and Space Administration.

Revisions:

Version 1.0 draft by Glynn Hulley, 11/11/2010

Contacts

Readers seeking additional information about this study may contact the following researchers:

- Glynn C. Hulley
  MS 183-501
  Jet Propulsion Laboratory
  4800 Oak Grove Dr.
  Pasadena, CA 91109
  Email: glynn.hulley@jpl.nasa.gov
  Office: (818) 354-2979
  Fax: (818) 354-5148

- Simon J. Hook
  MS 183-501
  Jet Propulsion Laboratory
  4800 Oak Grove Dr.
  Pasadena, CA 91109
  Email: simon.j.hook@jpl.nasa.gov
  Office: (818) 354-0974
  Fax: (818) 354-5148

Contents

Figures

Tables

1 Introduction

The Hyperspectral and Infrared Imager (HyspIRI) mission includes two instruments: a visible shortwave infrared (VSWIR) imaging spectrometer operating between 380 and 2500 nm in 10-nm contiguous bands and a thermal infrared (TIR) multispectral scanner with eight spectral bands operating between 4 and 13 µm, both at spatial scales of 60 m. The VSWIR and TIR instruments have revisit times of 19 and 5 days with swath widths of 145 and 600 km, respectively.

This document outlines the theory and methodology for generating the HyspIRI Level-2 TIR surface radiance product. The surface radiance is primarily used for monitoring changes in Earth's surface composition and will address many of the science and application questions in the Science Decadal Survey (NRC 2007) relating to volcanoes, fires, water usage, and urbanization. The surface radiance is primarily used as an input to the temperature-emissivity separation algorithm. Land surface temperature and emissivity are two important variables used for a variety of Earth Surface studies, including surface energy balance, land use, land cover change, drought monitoring, and the cryosphere. The radiance at sensor measured by the HyspIRI instrument will include atmospheric emission, scattering, and absorption by the Earth's atmosphere. These atmospheric effects need to be removed from the observation in order to isolate the land-leaving surface radiance contribution. The accuracy of the atmospheric correction is dependent upon accurate characterization of the atmospheric state using independent atmospheric profiles of temperature, water vapor, and other gas constituents (e.g., ozone). The profiles are typically input to a radiative transfer model for estimating atmospheric transmittance, path, and sky radiances. Once the residual effects of the atmosphere have been removed, it is possible to study seasonal and inter-annual changes with the data.

There are typically three approaches for atmospherically correcting data from TIR sensors. The first approach uses differential absorption characteristics of atmospheric water vapor in the longwave region using multiple bands or angles. Variations of this method include the split window (SW) approach (Coll and Caselles 1997; Prata 1994; Price 1984; Wan and Dozier 1996; Yu et al. 2008), the multichannel algorithm (Deschamps and Phulpin 1980), and the dual-angle algorithm (Barton et al. 1989). The surface emissivity effects are estimated by using land cover classification maps and assigning fixed emissivities based on cover type

(Snyder et al. 1998). In split-window algorithms, errors in longwave emissivity typically have a large effect on temperature accuracy and, depending on the water vapor content, are on average ~0.7 K for a band emissivity uncertainty of 0.005 (0.5%) (Galve et al. 2008). This type of approach will not be used for the HyspIRI standard algorithm for the three reasons it was not used for the Advanced Spaceborne Thermal Emission and Reflection Radiometer (ASTER) atmospheric correction algorithm (Palluconi et al. 1999): 1) The HyspIRI TIR bands 3–8 have been placed in the clearest regions of the atmospheric window; 2) the emissivity of the land surface is in general heterogeneous and is dependent on many factors, including surface soil moisture, vegetation cover changes, and surface compositional changes; and 3) split-window algorithms are inherently very sensitive to measurement noise between bands.

2 HyspIRI Instrument Characteristics

The TIR instrument will acquire data in eight spectral bands, seven of which are located in the thermal infrared part of the electromagnetic spectrum between 7 and 13 µm (Figure 1). The remaining band is located in the mid-infrared part of the spectrum around 4 um. The center position and width of each band is provided in Table 1. The spectral location of each band was based on the measurement requirements identified in the science traceability matrices, which included recognition that related data were acquired by other sensors such as ASTER and MODIS. However, the exact position of these bands has not been fully determined and is expected to be revised based on ongoing studies. The positions of three of the TIR bands closely match the first three thermal bands of ASTER, while two of the TIR bands match bands of ASTER and MODIS typically used for split-window type applications (ASTER bands 12–14 and MODIS bands 31, 32). It is expected that small adjustments to the band positions will be made based on ongoing science activities.

A key science objective for the TIR instrument is the study of hot targets (volcanoes and fires), so the saturation temperature for the 4-µm channel is set high (1200 K), whereas the saturation temperatures for the thermal infrared channels are set at 500 K.

The TIR instrument will operate as a whiskbroom mapper, similar to MODIS but with 256 pixels in the cross-whisk direction for each spectral channel (Figure 2). A conceptual layout for the instrument is shown in Figure 3. The scan mirror rotates at a constant angular speed. It sweeps the focal plane image across nadir, then to a blackbody target and space, with a 2.2- second cycle time.

The f/2 optics design is all reflective, with gold-coated mirrors. The 60 K focal plane will be single-bandgap mercury cadmium telluride, hybridized to a CMOS readout chip, with a butcher block spectral filter assembly over the detectors. Thirty-two analog output lines, each operating at 10–12.5 MHz, will move the data to analog-to-digital converters.

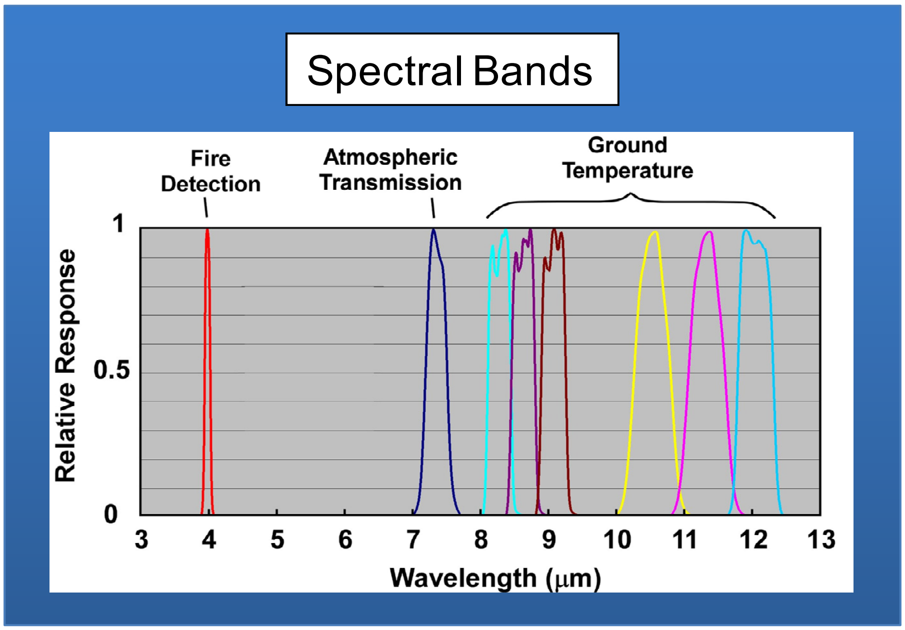

Figure 1: HyspIRI TIR instrument proposed spectral bands.

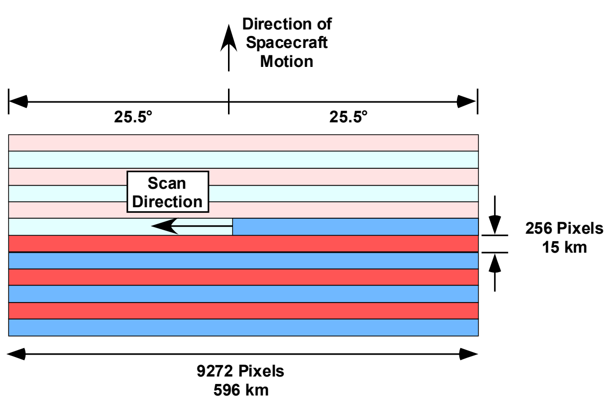

Figure 2: HyspIRI TIR scanning scheme.

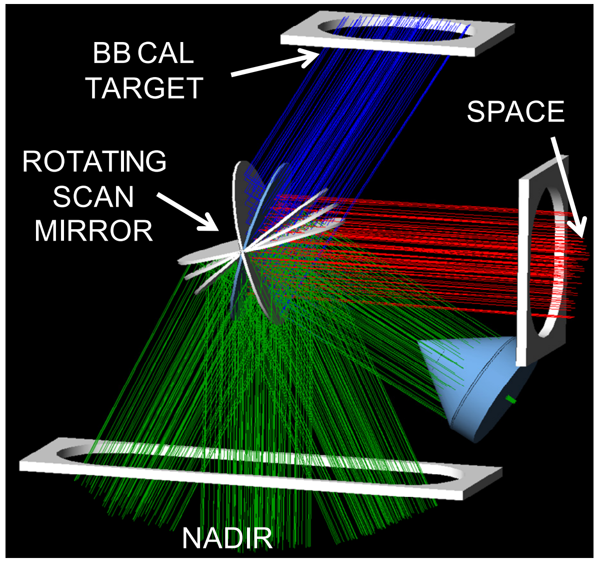

Figure 3: HyspIRI TIR conceptual layout.

The temperature resolution of the thermal channels is much finer than the mid-infrared channel, which, due to its high saturation temperature, will not detect a strong signal until the target is above typical terrestrial temperatures. All the TIR channels are quantized at 14 bits. Expected sensitivities of the eight channels, expressed in terms on noise-equivalent temperature difference, are shown in the following two plots (Figures 4 and 5).

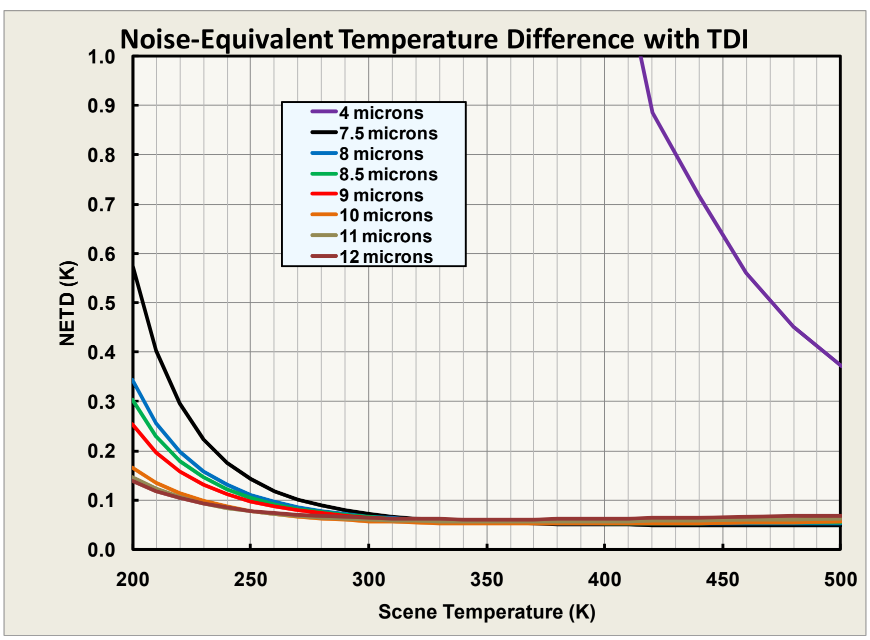

Figure 4: HyspIRI TIR predicted sensitivity 200–500 K.

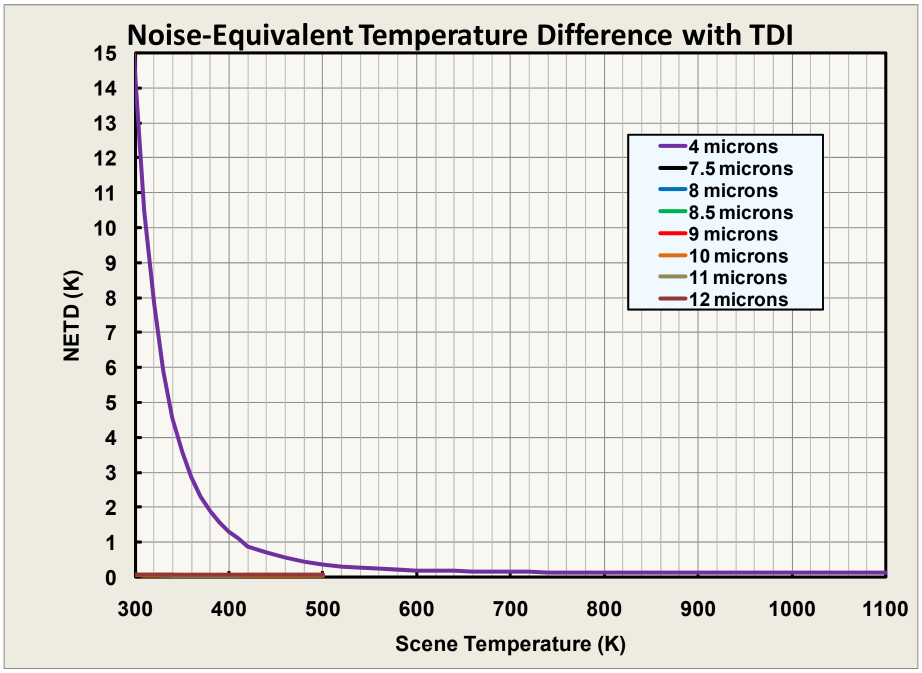

Figure 5: HyspIRI TIR predicted sensitivity 300–1100 K

The TIR instrument will have a swath width of 600 km with a pixel spatial resolution of 60 m, resulting in a temporal revisit of 5 days at the equator. The instrument will be on both day and night, and it will acquire data over the entire surface of the Earth. Like the VSWIR, the TIR instrument will acquire full spatial resolution data over the land and coastal oceans (to a depth of < 50 m but, over the open oceans, the data will be averaged to a spatial resolution of 1 km. The large swath width of the TIR will enable multiple revisits of any spot on the Earth every week (at least 1 day view and 1 night view). This repeat period is necessary to enable monitoring of dynamic or cyclical events such as volcanic hotspots or crop stress associated with water availability.

Table 1: Preliminary TIR Measurement Characteristics

Spectral	
Bands (8) µm	3.98 µm, 7.35 µm, 8.28 µm, 8.63 µm, 9.07 µm, 10.53 µm, 11.33 µm, 12.05 µm
Bandwidth	0.084 µm, 0.32 µm, 0.34 µm, 0.35 µm, 0.36 µm, 0.54 µm, 0.54 µm, 0.52 µm
Accuracy	<0.01 µm
Radiometric	
Range	Bands 2–8 = 200 K – 500 K; Band 1 = 1200 K
Resolution	< 0.05 K, linear quantization to 14 bits
Accuracy	< 0.5 K 3-sigma at 250 K
Precision (NEdT)	< 0.2 K
Linearity	>99% characterized to 0.1 %
Spatial	
IFOV	60 m at nadir
MTF	>0.65 at FNy
Scan Type	Push-Whisk
Swath Width	600 km (±25.5° at 623-km altitude)
Cross Track Samples	9,300
Swath Length	15.4 km (± 0.7 degrees at 623-km altitude)
Down Track Samples	256
Band to Band Co-Registration	0.2 pixels (12 m)
Pointing Knowledge	10 arcsec (0.5 pixels)
Temporal	
Orbit Crossing	11 a.m. Sun synchronous descending
Global Land Repeat	5 days at Equator
On Orbit Calibration	
Lunar views	1 per month {radiometric}
Blackbody views	1 per scan {radiometric}
Deep Space views	1 per scan {radiometric}
Surface Cal Experiments	2 (day/night) every 5 days {radiometric}
Spectral Surface Cal Experiments	1 per year
Data Collection	
Time Coverage	Day and Night
Land Coverage	Land surface above sea level
Water Coverage	Coastal zone minus 50 m and shallower
Open Ocean	Averaged to 1-km spatial sampling
Compression	2:1 lossless

3 Theory and Methodology

The radiometric accuracy and precision of the HyspIRI TIR instrument will be 0.5 K and 0.2 K, respectively for the thermal infrared bands. This radiometric accuracy will be ensured by using an on-board blackbody and view to space included as part of every 2.2-second sweep (15.4 km × 600 km on the ground). The expected accuracy of the measured radiance, expressed in terms of brightness temperature, is expected to be less than 0.5 K. The goal of the atmospheric correction then is to keep the residual errors from atmospheric effects to a minimum in order to maintain the 1 K or less accuracy for the surface radiance product.

3.1 TIR Radiative Transfer Background

The at-sensor measured radiance in the TIR spectral region (7–14 µm) is a combination of three primary terms: the Earth-emitted radiance, reflected downwelling sky irradiance, and atmospheric path radiance. Reflected solar radiation in the TIR region is negligible (Figure 6) and a much smaller component than the surface-emitted radiance. The reflected sky irradiance term is also generally smaller in magnitude than the surface-emitted radiance but needs to be taken into account, particularly on humid days when atmospheric water vapor contents are high. Given the small sky irradiance contribution and low reflectances in the TIR region for most types of surfaces, we can use the Lambertian surface assumption. Furthermore, the Lambertian assumption will not produce large errors since the HyspIRI instrument maximum view angle will be ±25.5°. Assuming the spectral variation in emissivity is small, and using Kirchhoff's law to express the hemispherical-directional reflectance as directional emissivity ($\rho_\lambda = 1 - \epsilon_\lambda$), the clear sky at-sensor radiance can be written as:

$$L_\lambda(\theta) = \left[\epsilon_\lambda B_\lambda(T_s) + (1 - \epsilon_\lambda) L_\lambda^{\downarrow}\right] \tau_\lambda(\theta) + L_\lambda^{\uparrow}(\theta), \quad (1)$$

where:

$L_\lambda(\theta)$ At-sensor radiance

λ Wavelength

θ Observation angle

ϵ_λ Surface emissivity

$B_\lambda(T_s)$ Planck function

T_s Surface temperature

$L_\lambda^{\downarrow}$ Downwelling sky irradiance

$\tau_\lambda(\theta)$ Atmospheric transmittance

$L_\lambda^{\uparrow}(\theta)$ Atmospheric path radiance

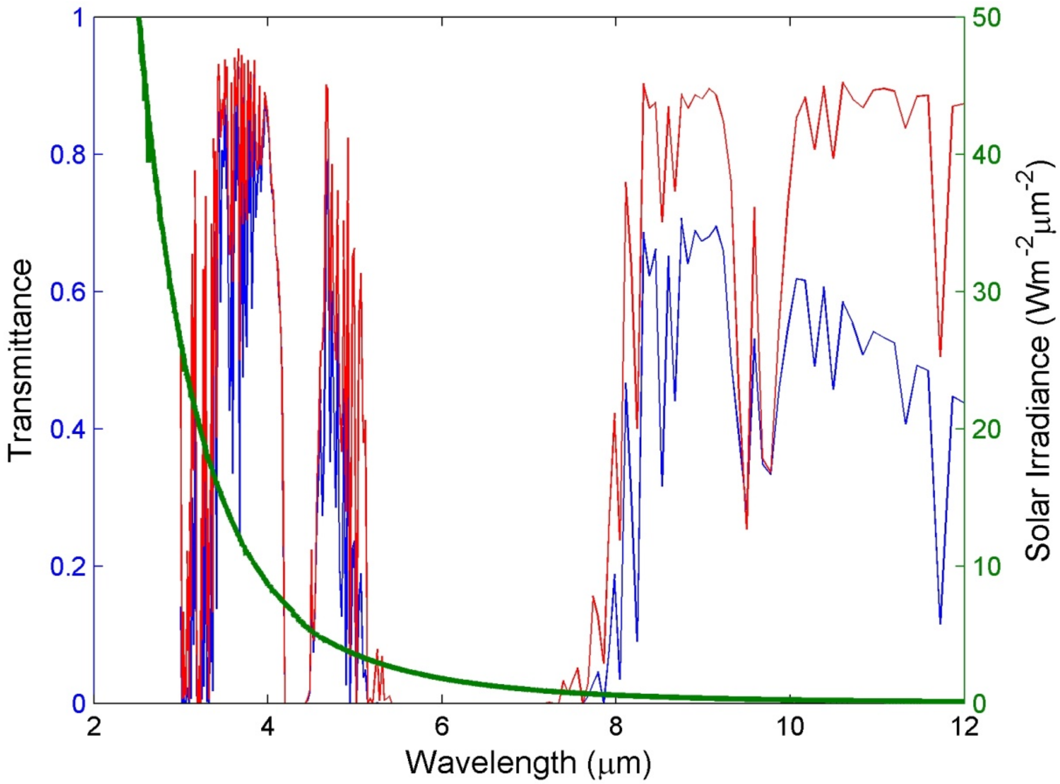

Figure 6: Simulated atmospheric transmittance for a US Standard Atmosphere (red) and tropical atmosphere (blue) in the 3–12 µm region. Also shown is the solar irradiance contribution W/m^2/µm^2.

Figure 7 shows the relative contributions from the surface-emission term, surface radiance, and at-sensor radiance for a US Standard Atmosphere, quartz emissivity spectrum, and surface temperature set to 300 K. Vertical bars show the placement of the eight HyspIRI MWIR and TIR bands. The reflected downwelling term adds a small contribution in the window regions but will become more significant for more humid atmospheres. The at-sensor radiance shows large departures from the surface radiance in regions where atmospheric absorption from gases such as CO_2, H_2O, and O_3 are high.

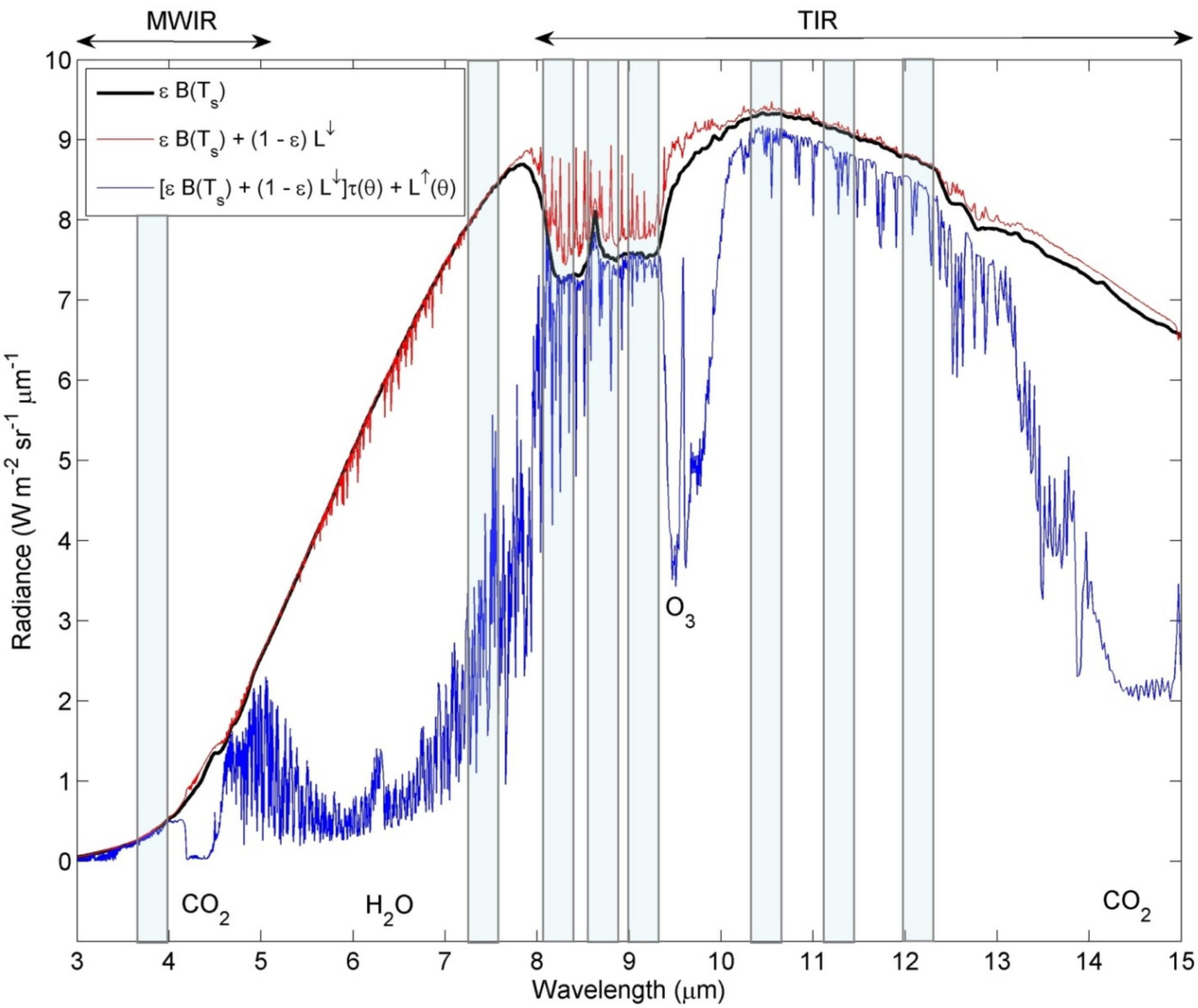

Figure 7: Radiance simulations of the surface-emitted radiance, surface-emitted and reflected radiance, and at-sensor radiance using the MODTRAN 5.2 radiative transfer code, US Standard Atmosphere, quartz emissivity spectrum, surface temperature = 300K, and viewing angle set to nadir. Vertical bars show placements of the HyspIRI MWIR and TIR bands.

The at-sensor radiance for a discrete band i is obtained by weighting and normalizing the at-sensor spectral radiance calculated by equation (1) with the sensor's spectral response function for each band, Sr_λ as follows:

$$L_i(\theta) = \frac{\int Sr_\lambda(\mathrm{i}) \cdot L_\lambda(\theta) \cdot \mathrm{d}\lambda}{Sr_\lambda(\mathrm{i}) \cdot \mathrm{d}\lambda} \tag{2}$$

Using equations (1) and (2), the surface radiance for band i can be written as a combination of two terms: Earth-emitted radiance, and reflected downward irradiance from the sky and surroundings:

$$L_{s,i} = \epsilon_i B_i(T_s) + (1-\epsilon_i)L_i^{\downarrow} = \frac{L_i(\theta) - L_i^{\uparrow}(\theta)}{\tau_i(\theta)} \tag{3}$$

The atmospheric parameters ($L_\lambda^{\downarrow}$, $\tau_\lambda(\theta)$, $L_\lambda^{\uparrow}(\theta)$) are estimated with a radiative transfer model such as MODTRAN (Berk et al. 2005; Kneizys et al. 1996a) using input atmospheric fields of air temperature, relative humidity, and geopotential height.

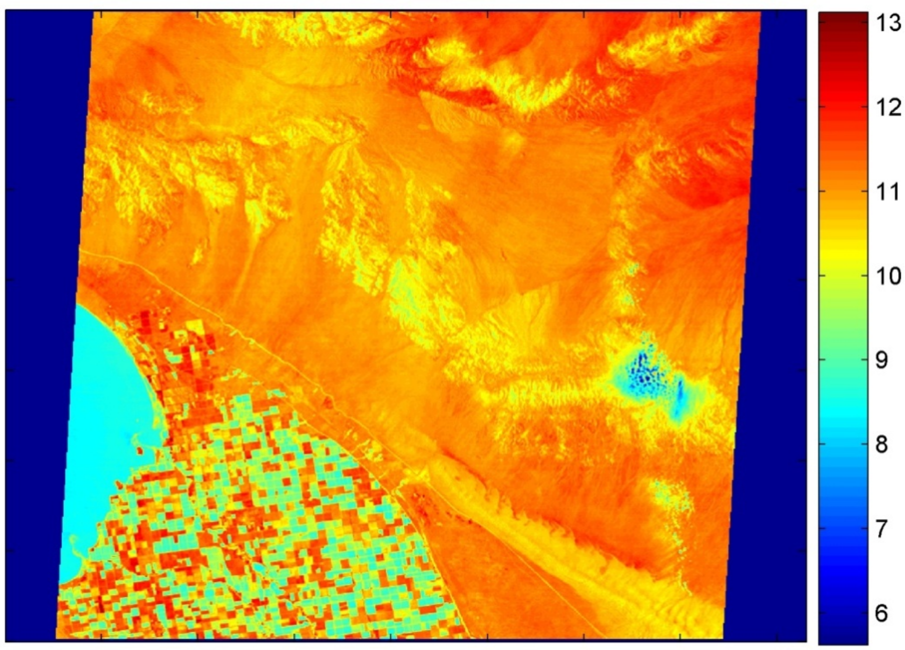

Figure 8: ASTER at-sensor radiance image at 90-m spatial resolution over the Salton Sea and Algodones dunes area in southeastern California on June 15, 2000. Radiances are in W/m^2/sr/µm.

The approach for computing surface radiance is essentially a two-step process. First, the atmospheric state is characterized by obtaining atmospheric profiles of air temperature, water vapor, geopotential height, and ozone at the observation time and location of the measurement. Ideally, the profiles should be obtained from a validated, mature product with sufficient spatial resolution and close enough in time with the HyspIRI observation to avoid interpolation errors. This is particularly important for the temperature and water profiles to ensure good accuracy.

Absorption from other gas species such as CH_4, CO, and N_2O will not be significant for the placement of the HyspIRI TIR bands. The second step is to input the atmospheric profiles to a radiative transfer model to estimate the atmospheric parameters defined previously. This method will be used on clear-sky pixels only, which will be classified using a cloud mask specifically tailored for HyspIRI data. Clouds result in strong attenuation of the thermal infrared signal reaching the sensor, and an attempt to correct for this attenuation will not be made.

3.2 Radiative Transfer Model

The current choice of radiative transfer model is the latest version of the Moderate Resolution Atmospheric Radiance and Transmittance Model (MODTRAN) (Berk et al. 2005). MODTRAN has been sufficiently tested and validated and meets the speed requirements necessary for high spatial resolution data processing. The most recent MODTRAN 5.2 uses an improved molecular band model, termed the Spectrally Enhanced Resolution MODTRAN (SERTRAN), which has a much finer spectroscopy (0.1 cm^{-1}) than its predecessors (1-2 cm^{-1}), resulting in more accurate modeling of band absorption features in the longwave TIR window regions (Berk et al. 2005). Furthermore, validation with Line-by-Line models (LBL) has shown good accuracy.

Older versions of MODTRAN, such as version 3.5 and 4.0, have been used extensively in the past few decades for processing multi-band and broadband TIR and short-wave/visible imaging sensors such as ASTER data on NASA's Terra satellite. Earlier predecessors, such as MODTRAN 3.5, used a molecular band model with 2 cm^{-1} resolution and traced their heritage back to previous versions of LOWTRAN (Berk 1989; Kneizys et al. 1996b). With the next generation's state-of-the-art, mid- and longwave IR hyperspectral sensors due for launch in the next decade, there has been greater demand for higher resolution and quality radiative transfer modeling. MODTRAN 5.2 has been developed to meet this demand by reformulating the MODTRAN molecular band model line center and tail absorption algorithms. Further improvements include the auxiliary species option, which simulates the effects of HITRAN-specific trace molecular gases and a new multiple scattering option, which improves the accuracy of radiances in transparent window regions.

Wan and Li (2008) have compared MODTRAN 4 simulations with clear-sky radiances from a well-calibrated, advanced Bomem TIR interferometer (MR100) and found accuracies to within 0.1 K for brightness temperature-equivalent radiance values.

3.3 Atmospheric Profiles

The general methodology for atmospherically correcting HyspIRI TIR data will be based largely on the methods that were developed for the ASTER instrument (Palluconi et al. 1999), which has a similar spatial (90-m) and spectral resolution (5 TIR bands) to HyspIRI. However, significant improvements will be made by taking advantage of newly developed techniques and more advanced algorithms to improve accuracy. Currently two options for atmospheric profile sources are available: 1) interpolation of data assimilated from Numerical Weather Prediction (NWP) models, and 2) retrieved atmospheric geophysical profiles from remote-sensing data. The NWP models use current weather conditions, observed from various sources (e.g., radiosondes, surface observations, and weather satellites) as input to dynamic mathematical models of the atmosphere to predict the weather. Data are typically output in 6-hour increments, e.g., 00, 06, 12, and 18 UTC. Examples include the Global Data Assimilation System (GDAS) product provided by the National Centers for Environmental Prediction (NCEP) (Kalnay et al. 1990), the Modern Era Retrospective-analysis for Research and Applications (MERRA) product provided by the Goddard Earth Observing System Data Assimilation System Version 5.2.0 (GEOS-5.2.0) (Bosilovich et al. 2008), and the European Center for Medium-Range Weather Forecasting (ECMWF), which is supported by more than 32 European states. Remote-sensing data, on the other hand, are available real-time, typically twice daily and for clear-sky conditions. The principles of inverse theory are used to estimate a geophysical state (e.g., atmospheric temperature) by measuring the spectral emission and absorption of some known chemical species such as carbon dioxide in the thermal infrared region of the electromagnetic spectrum (i.e., the observation). Examples of current remote sensing data include the Atmospheric Infrared Sounder (AIRS) (Susskind et al. 2003) and Moderate Resolution Imaging Spectroradiometer (MODIS) (Justice and Townshend 2002), both on NASA's Aqua satellite launched in 2002.

The standard ASTER atmospheric correction technique, which is operated at the Land Processes Distributed Active Archive Center (LP DAAC) at the EROS Center in Sioux Falls, SD, uses input atmospheric profiles from the NCEP GDAS product at 1° spatial resolution and 6-hour intervals. An example of NCEP profiles of relative humidity and air temperature at 20 levels in the atmosphere is shown in Figure 9. An interpolation scheme in both space and time is required to characterize the atmospheric conditions for an ASTER image on a pixel-by-pixel basis. This method could potentially introduce large errors in estimates of air temperature and water vapor, especially in humid regions where atmospheric water vapor can vary on smaller spatial scales than 1°. The propagation of these atmospheric correction errors would result in band-dependent surface radiance errors in both spectral shape and magnitude, which in turn would result in errors of retrieved Level-2 products such as surface emissivity and temperature. A second option for ASTER was to use atmospheric profiles from the MODIS joint atmospheric Level-2 product, MOD07 (Seemann et al. 2003). The MOD07 product consists of profiles of temperature and moisture produced at 20 standard levels and total precipitable water vapor (TPW), total ozone, and skin temperature, produced at 5×5 MODIS 1-km pixels and coincident with the ASTER observations on Terra. Initially the MODIS profile option was the data source of choice; however, the profiles were never incorporated due to a lack of validation and testing during the first few years of Terra launch. The latest MOD07 algorithm update (v5.2) includes a new and improved surface emissivity training data set, with the result that RMSE differences in TPW between MOD07 and a microwave radiometer (MWR) at the Atmospheric Radiation Measurement (ARM) Southern Great Plains (SGP) site in Oklahoma were reduced from 2.9 mm to 2.5 mm (Seemann et al. 2008). Other validation campaigns have included comparisons with ECMWF and AIRS data, radiosonde observations (RAOBS), and MWR data at ARM SGP.

The plan for HyspIRI will be to utilize atmospheric profiles generated from remote-sensing data close in time to the HyspIRI observation time (10:30 UTC equator crossing time) over the course of the mission. With the expected launch of HyspIRI still more than 10 years away, it is difficult to forecast what appropriate remote-sensing data will be available during that time. Profile data will need to be close in time (preferably < 0.5 hr) to the HyspIRI observation as clouds and water vapor distributions can change rapidly over short periods depending on the local weather conditions (e.g., wind).

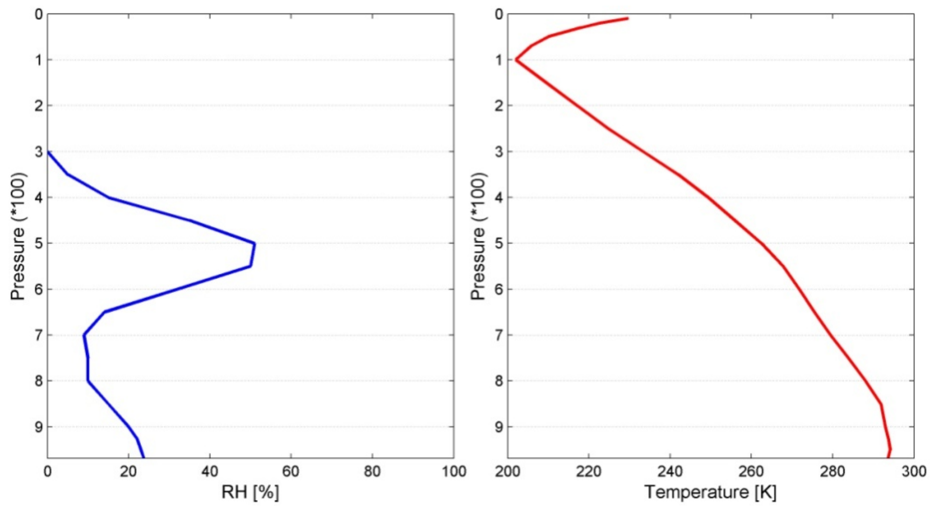

Figure 9: Profiles of Relative Humidity (RH) and Air Temperature from the NCEP GDAS product.

As a backup, we will have NWP model data ready to be ingested and interpolated into the atmospheric correction system. NCEP and MERRA data, for example, would be easily accessible and available during the course of the HyspIRI mission. In order to improve accuracy of the water vapor profiles, an estimate of the total precipitable water vapor (PWV) will be obtained from HyspIRI's hyperspectral imaging spectrometer and used to scale the water vapor profile data from the NWP or remote-sensing profile source. This will greatly improve the accuracy of the atmospheric correction especially if NWP model data, or remote sensing data not close in time to the HyspIRI observation, are used.

3.4 Radiative Transfer Sensitivity Analysis

The accuracy of the atmospheric correction technique proposed relies on the accuracy of the input variables to the model, such as air temperature, relative humidity, and ozone. The combined uncertainties of these input variables need to be known if an estimate of the radiative transfer accuracy is to be estimated. These errors can be band dependent, since different channels have different absorbing features and they are also dependent on absolute accuracy of the input profile data at different levels. The final uncertainty introduced is the accuracy of the radiative transfer model itself; however, this is expected to be small.

To perform the analysis, four primary input geophysical parameters were input to MODTRAN 5.2, and each parameter was changed sequentially in order to estimate the corresponding percent change in radiance (Palluconi et al. 1999). These geophysical parameters were air temperature, relative humidity, ozone, and aerosol visibility. Two different atmospheres were chosen, a standard tropical atmosphere and a mid-latitude summer atmosphere. These two simulated atmospheres should capture realistic errors we expect to see in humid conditions.

Typical values for current infrared sounder accuracies (e.g., AIRS) of air temperature and relative humidity retrievals in the boundary layer were used for the perturbations: 1) air temperature of 2 K, 2) relative humidity of 20%, 3) ozone was doubled, and 3) aerosol visibility was changed from rural to urban class. Numerical weather models such as NCEP would most likely have larger uncertainties in the 1–2 K range for air temperature and 10–20% for relative humidity (Kalnay et al. 1990), but it is expected that infrared sounder retrievals will be available for the atmospheric correction during the HyspIRI mission, for example, NOAA's Joint Polar Satellite System (JPSS), which will launch sometime in the 2015–2018 timeframe.

Table 2 shows the results for three simulated HyspIRI bands 3, 5 and 7, expressed as percent change in radiance. HyspIRI-TIR bands 3 and 5 correspond to band-integrated values for ASTER bands 10 and 12, and HyspIRI-TIR band 7 corresponds to MODIS band 31. Figure 7 shows that band 3 falls closest to the strong water vapor absorption region below about 8 µm, so we expect this band to be most sensitive to changes in atmospheric water vapor, and to a lesser extent the air temperature. The results show that band 3 is in fact most sensitive to perturbations in relative humidity. The temperature perturbations have similar effects for bands 3 and 5 for both atmospheres and are lower for band 7. Doubling the ozone results in a much larger sensitivity for band 5, since it is closest to the strong ozone absorption feature centered around the 9.5-µm region as shown in Figure 7. Changing the aerosol visibility from rural to urban had a small effect on each band but was largest for band 5. Generally the radiance in the thermal infrared region is insensitive to aerosols in the troposphere so, for the most part, a climatology-based estimate of aerosols would be sufficient. However, when stratospheric aerosol amounts increase substantially due to volcanic eruptions, for example, then aerosols amounts from future NASA remote-sensing missions such as ACE and GEO-CAPE would need to be taken into account.

It should also be noted, as discussed in Palluconi et al. (1999), that in reality these types of errors may have different signs, change with altitude, and/or have cross-cancelation between the parameters. As a result, it is difficult to quantify the exact error budget for the radiative transfer calculation; however, what we do know is that the challenging cases will involve warm and humid atmospheres where distributions of atmospheric water vapor are the most uncertain.

Table 2: Percent changes in simulated at-sensor radiances for changes in input geophysical parameters, with equivalent change in brightness temperature shown in parentheses.

Geophysical Parameter	Change in Parameter	% Change in Radiance (Tropical Atmosphere)			% Change in Radiance (Mid-lat Summer Atmosphere)		
		Band 3 (8.3 μm)	Band 5 (9.1 μm)	Band 7 (11 μm)	Band 3 (8.3 μm)	Band 5 (9.1 μm)	Band 7 (11 μm)
Air Temperature	+2 K	-2.72 (1.32 K)	-2.86 (1.56 K)	-2.07 (1.40 K)	-3.16 (1.50 K)	-3.25 (1.72 K)	-2.54 (1.68 K)
Relative Humidity	+20%	3.1 (1.94 K)	1.91 (1.06 K)	2.26 (1.55 K)	2.88 (1.39 K)	1.03 (0.55 K)	0.83 (0.56 K)
Ozone	× 2	0.10 (0.05 K)	2.18 (1.19 K)	0.00 (0.00 K)	0.11 (0.05 K)	1.12 (1.11 K)	0.00 (0.00 K)
Aerosol	Urban/Rural	0.33 (0.16 K)	0.51 (0.28 K)	0.27 (0.18 K)	0.33 (0.16 K)	0.53 (0.28 K)	0.29 (0.19 K)

4 Water Vapor Scaling (WVS) Method

The accuracy of the ASTER Temperature Emissivity Separation (TES) algorithm is limited by uncertainties in the atmospheric correction, which results in a larger apparent emissivity contrast. This intrinsic weakness of the TES algorithm has been systemically analyzed by several authors (Coll et al. 2007; Gillespie et al. 1998; Gustafson et al. 2006; Hulley and Hook 2009; Li et al. 1999), and its effect is greatest over graybody surfaces that have a true spectral contrast that approaches zero. In order to minimize atmospheric correction errors, a Water Vapor Scaling (WVS) method has been introduced to improve the accuracy of the water vapor atmospheric profiles on a band-by-band basis for each observation using an Extended Multi-Channel/Water Vapor Dependent (EMC/WVD) algorithm (Tonooka 2005), which is an extension of the Water Vapor Dependent (WVD) algorithm (Francois and Ottle 1996). The EMC/WVD equation models the at-surface brightness temperature, given the at-sensor brightness temperature, along with an estimate of the total water vapor amount:

$$T_{g,i} = \alpha_{i,0} + \sum_{k=1}^{n} \alpha_{i,k} T_k \tag{4}$$

$$\alpha_{i,k} = p_{i,k} + q_{i,k} W + r_{i,k} W^2,$$

where:

i Band number

n Number of bands

W Estimate of total precipitable water vapor (cm)

p, q, r Regression coefficients for each band

T_k Brightness temperature for band k, [K]

$T_{g,i}$ Brightness surface temperature for band, i

The coefficients of the EMC/WVD equation are determined using a global-based simulation model with data typically from model data, such as the NCEP Climate Data Assimilation System (CDAS) reanalysis project (Tonooka 2005).

The scaling factor, γ, used for improving a water profile, is based on the assumption that the transmissivity, τ_i, can be express by the Pierluissi double exponential band model formulation. The scaling factor is computed for each gray pixel on a scene using $T_{g,i}$ computed from equation (4) and τ_i computed using two different γ values that are selected *a priori*:

$$\gamma^{\alpha_i} = \frac{\ln\left(\frac{\tau_i(\theta,\gamma_2)^{\gamma_1{}^{\alpha_i}}}{\tau_i(\theta,\gamma_1)^{\gamma_2{}^{\alpha_i}}} \cdot \left(\frac{B_i\left(T_{g,i}\right) - L_i^{\uparrow}(\theta,\gamma_1)/(1-\tau_i(\theta,\gamma_1))}{L_i - L_i^{\uparrow}(\theta,\gamma_1)/(1-\tau_i(\theta,\gamma_1))}\right)^{\gamma_1{}^{\alpha_i} - \gamma_2{}^{\alpha_i}}\right)}{\ln(\tau_i(\theta,\gamma_2)/\tau_i(\theta,\gamma_1))} \tag{5}$$

where:

α_i Band model parameter

γ_1, γ_2 Two appropriately chosen γ values

$\tau_i\left(\theta,\gamma_{1,2}\right)$ Transmittance calculated with water vapor profile scaled by γ

$L_i^{\uparrow}\left(\theta,\gamma_{1,2}\right)$ Path radiance calculated with water vapor profile scaled by γ

Typical values for γ are $\gamma_1 = 1$, and $\gamma_2 = 0.7$. Tonooka (2005) found that the γ calculated by equation (3) will not only reduce biases in the water vapor profile, but will also simultaneously reduce errors in the air temperature profiles and/or elevation. An example of the water vapor scaling factor, γ, is shown in Figure 10 for an ASTER scene over the Algodones dunes area on June 15, 2000.

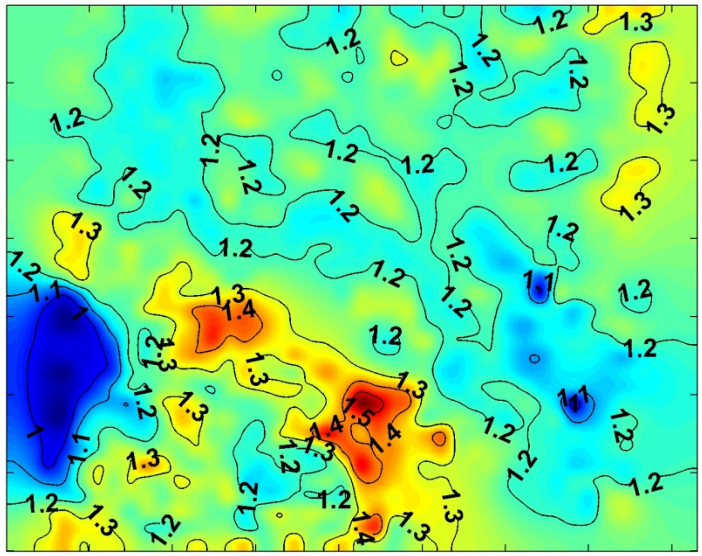

Figure 10: Water Vapor Scaling (WVS) factor, γ, computed using equation (5) for the ASTER radiance image shown in Figure 8. The atmospheric parameters were computed using MODIS MOD07 atmospheric profiles at 5 km spatial resolution and MODTRAN 5.2 radiative transfer code. The image has been interpolated and smoothed as discussed in the text.

4.1 Gray Pixel Computation

It is important to note that γ is only computed for graybody pixels (e.g., vegetation, water, and some soils) with emissivities close to 1.0 and, as a result, an accurate gray-pixel estimation method is required prior to processing. Vegetation indices such as the Normalized Difference Vegetation Index (NDVI), land cover databases (e.g., MODIS MOD12), and thermal log residuals (TLR) (Hook et al. 1992), are three different approaches that can be used in combination with each other to accomplish this. Typically, one classifies all green vegetation pixels first by thresholding NDVI computed from the VSWIR bands. Water and snow/ice pixels are then classified using a land-water and snow-cover map. The MODIS product, for example, produces both these types of products at 1-km resolution (e.g., MOD10 and MOD44). Using these gray pixels as a first-guess estimate, a TLR approach can then be used to further refine the gray-pixel map. The TLR approach spectrally enhances images generated from multi-spectral data and removes dependence on band-independent parameters such as surface temperature. All gray pixels within a TLR image will have similar spectral shapes, and this characteristic is exploited in order to refine the gray-pixel map from the first guess gray pixels. Figure 11 shows an example of a gray-pixel map for an ASTER image from Figure 8.

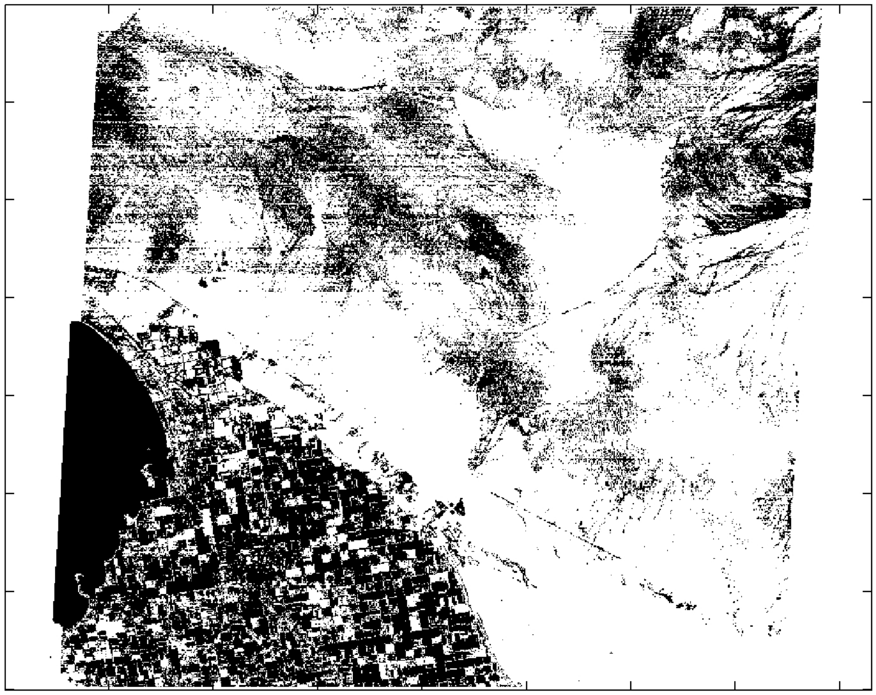

Figure 11: Gray-pixel map for the Salton Sea ASTER image (black=gray, white=bare). A first guess gray-pixel map was first estimated by thresholding ASTER reflectance indices (e.g., NDVI), and then refined using the Thermal Log Residual (TLR) method described in the text.

4.2 Interpolation and Smoothing

Once γ is computed for all gray pixels, the values are horizontally interpolated to adjacent bare pixels on the scene and smoothed before computing the improved atmospheric parameters. An inverse distance-weighted interpolation method is typically used to fill in bare pixel gaps. This is an interpolation method frequently used in numerical weather forecasting with much success. The specific steps for interpolation of γ values are as follows:

1. First all bare pixels are set to 1; in addition, all γ values less than 0.2 and greater than 3 are set to 1 for stability purposes and to eliminate possible cloud contamination.
2. Next, all cloudy pixels on the scene are set to NaN.
3. All bare pixels are then looped over, and optimum weights are found for all gray pixels within a given effective radius of the bare pixel. The γ value for the pixel is

then computed using the weighted γ values surrounding the pixel and ignoring all NaN values as follows:

$$\gamma(x, y) = \sum_{i=1}^{n} w_i \gamma_i \tag{6}$$

where n is the number of gray pixels, and w_i are the weight functions assigned to each gray pixel γ value:

$$w_i = \frac{d_i^{-p}}{\sum_{j=1}^{n} d_j^{-p}} \tag{7}$$

where p is weighting factor called the power parameter, typically equal to 2. Higher values give larger weights to the closest pixels. d_i is the geometrical distance from the interpolation pixel to the scattered points of interest within some effective radius:

$$d_i = \sqrt{(\mathrm{x} - \mathrm{x_i})^2 + (\mathrm{y} - \mathrm{y_i})^2} \tag{8}$$

where x and y are the coordinates of the interpolation point, and x_i and y_i are coordinates of the scattered points.

4. If any bare pixels remain after the first pass, the bare pixels with a valid, calculated γ value are considered gray pixels, and the process is repeated until γ values for all bare pixels have been computed.

This interpolation method should not introduce large error, since gray pixels are usually widely available in any given scene and atmospheric profiles do not change significantly at the medium-range scale (~50 km). Figure 10 shows an example of a γ image after interpolation and smoothing.

4.3 Scaling Atmospheric Parameters

4.3.1 Transmittance and Path Radiance

Once the MODTRAN run has completed and the γ image has been interpolated and smoothed, the atmospheric parameters transmittance τ_i and path radiance $L_i^{\uparrow}$ are modified as follows:

$$\tau_i(\theta,\gamma) = \tau_i(\theta,\gamma_1)^{\frac{\gamma^{\alpha_i}-\gamma_2{}^{\alpha_i}}{\gamma_1{}^{\alpha_i}-\gamma_2{}^{\alpha_i}}} \cdot \tau_i(\theta,\gamma_2)^{\frac{\gamma_1{}^{\alpha_i}-\gamma^{\alpha_i}}{\gamma_1{}^{\alpha_i}-\gamma_2{}^{\alpha_i}}} \tag{9}$$

$$L_i^{\uparrow}(\theta,\gamma) = L_i^{\uparrow}(\theta,\gamma_1) \cdot \frac{1-\tau_i(\theta,\gamma)}{1-\tau_i(\theta,\gamma_1)} \tag{10}$$

Once the transmittance and path radiance have been adjusted using the scaling factor, the surface radiance can be computed using equation (2).

4.3.2 Downward Sky Irradiance

In the WVS simulation model, the downward sky irradiance can be modeled using the path radiance, transmittance, and view angle as parameters. To simulate the downward sky irradiance in a MODTRAN run, the sensor target is placed a few meters above the surface, with surface emission set to zero, and view angle set at prescribed angles, e.g., Gaussian angles (θ = 0°, 11.6°, 26.1°, 40.3°, 53.7°, and 65°). In this way, the only radiance contribution is from the reflected downwelling sky irradiance at a given view angle. The total sky irradiance contribution is then calculated by summing up the contribution of all view angles over the entire hemisphere:

$$L_i^{\downarrow} = \int_0^{2\pi}\int_0^{\pi/2} L_i^{\downarrow}(\theta) \cdot sin\theta \cdot cos\theta \cdot d\theta \cdot d\delta \tag{11}$$

where θ is the view angle and δ is the azimuth angle. However, to minimize computational time in the MODTRAN runs, the downward sky irradiance can be modeled as a non-linear function of path radiance at nadir view:

$$L_i^{\downarrow}(\gamma) = a_i + b_i \cdot L_i^{\uparrow}(0,\gamma) + c_i L_i^{\uparrow}(0,\gamma)^2 \tag{12}$$

where a_i, b_i, and c_i are regression coefficients, and $L_i^{\uparrow}(0,\gamma)$ is computed by:

$$L_i^{\uparrow}(0,\gamma) = L_i^{\uparrow}(\theta,\gamma) \cdot \frac{1-\tau_i(\theta,\gamma)^{cos\theta}}{1-\tau_i(\theta,\gamma)} \tag{13}$$

Tonooka (2005) found RMSEs of less than 0.07 W/m^2/sr/µm for ASTER bands 10–14 when using equation (10) as opposed to equation (9). Figure 12 shows an example of comparisons between ASTER band 10 (8.3 µm) atmospheric transmittance (top), path radiance (middle), and computed surface radiance (bottom), before and after applying the WVS scaling factor, γ, for the ATER scene on June 15, 2000.

4.4 Determining EMC/WVD Coefficients

The EMC/WVD coefficients, p, q, r, from equation (2) are determined using a global simulation model with input atmospheric parameters from either numerical weather model or radiosonde data. Radiosonde databases such as the TIGR, SeeBor, and CLAR contain uniformly distributed global atmospheric soundings acquired both day and night in order to capture the full-scale natural atmospheric variability.

Geophysical profiles of air temperature, relative humidity, and geopotential height are used in combination with surface temperature and emissivity to simulate at-sensor brightness temperatures for the global set of profiles distributed uniformly over land. The air temperature profiles are then shifted by -2, 0, and +2 K, while the humidity profiles are scaled by factors of 0.8, 1.0, and 1.2. These types of perturbations will help simulate a full range of atmospheric conditions. Furthermore, the surface temperatures are modified by -5, 0, 5, and 10 K, and the surface emissivity provided consists of a set of 10 spectra typically from gray materials; for example, water, vegetation, snow, ice, and some types of soils. These emissivity spectra typically have values greater than 0.95. This ensures that the simulation results are not affected by uncertainties in surface emissivity, such as Lambertian effects. The at-sensor radiance is then computed using MODTRAN for the full set of profiles and perturbations ($3 \times 3 \times 4 \times 10 = 360$). The surface elevation is taken from a global DEM (e.g. ASTER GDEM), and the view angle is assumed to be nadir. Furthermore, a noise-equivalent differential temperature ($NE\Delta T$) appropriate for the sensor is applied using a normalized random number generator. Using the simulated at-sensor T_k, at-surface T_g brightness temperatures, and an estimate of the total precipitable water vapor, the coefficients in equation (2) can be found by using a linear least squares method.

NOTE: Since the HyspIRI band placements and spectral response functions in the TIR have not yet been fully decided upon, the EMC/WVD coefficients will be computed at a later date. The simulation model, however, is complete and ready for processing.

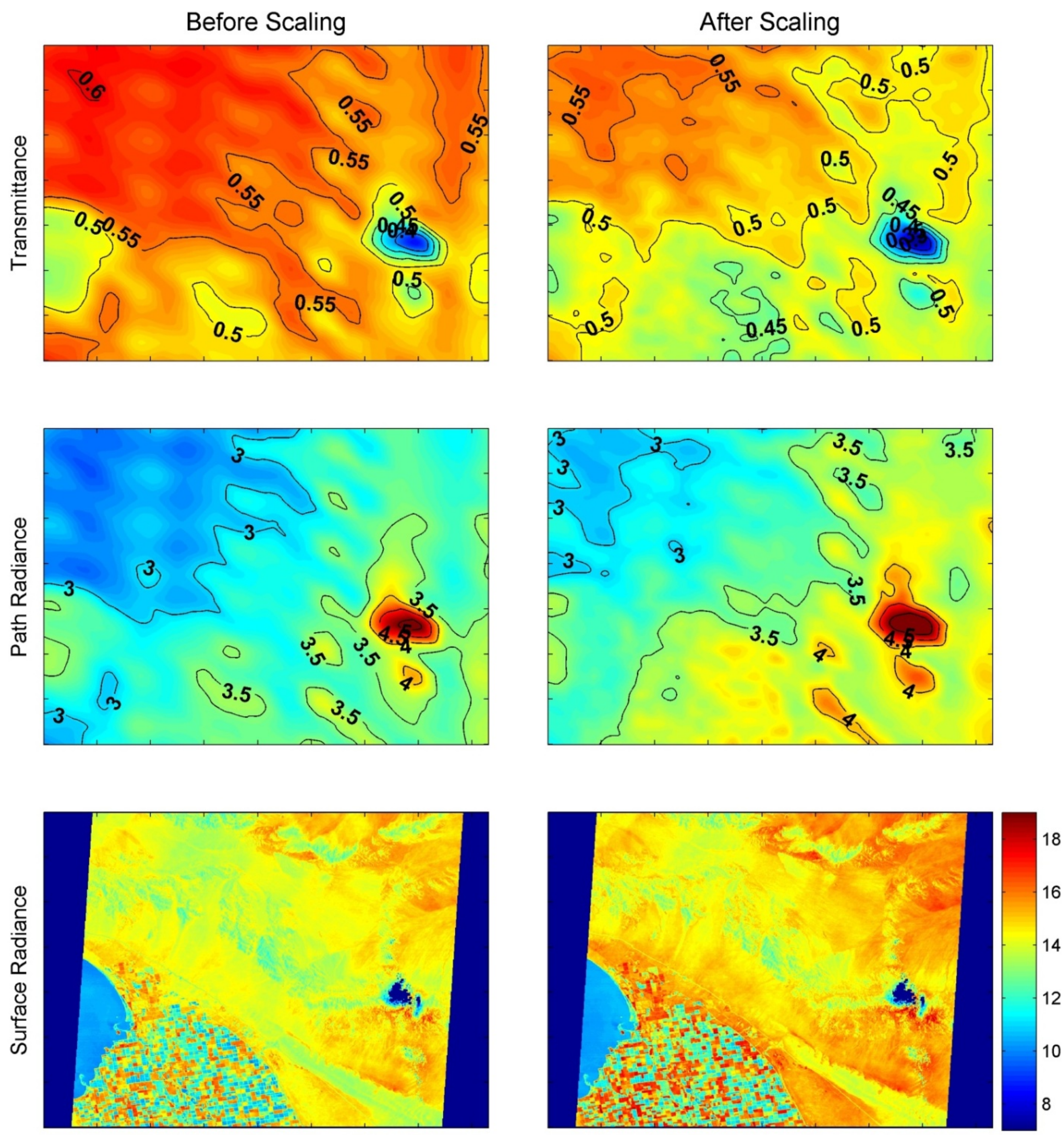

Figure 12: Comparisons between the atmospheric transmittance (top), path radiance (middle), and computed surface radiance (bottom), before and after applying the WVS scaling factor γ for the ASTER Algodones dunes scene. Results are shown for ASTER band 10 (8.3 µm), which will be comparable to HyspIRI TIR band 3 (8.3 µm).

4.5 Error Analysis

Once the EMC/WVD coefficients are computed, an error analysis is necessary to gauge performance under difficult conditions. RMSEs between the actual at-surface brightness temperature and modeled temperature using equation (2) need to be analyzed for dependence on input PWV values, surface temperatures and, more importantly, the emissivity. An error analysis by (Tonooka 2005) showed that emissivity had the largest dependence, particularly when using minimum emissivities less than 0.95. Therefore, careful attention needs to be made in choosing appropriate gray pixels when applying the WVS method.

Using 183 ASTER scenes over lakes, rivers, and sea surfaces, it was found that using the WVS method instead of the standard atmospheric correction improved estimates of surface temperature from 3–8 K in regions of high humidity (Tonooka 2005). These are substantial errors when considering the required accuracy of the TES algorithm is ~1 K (Gillespie et al. 1998).

5 Calibration and Validation

5.1 Pre-launch

Pre-launch validation activities for the HyspIRI TIR atmospheric correction algorithm will involve testing and validation of the radiative transfer model (e.g., MODTRAN) and input atmospheric profiles.

The current version of MODTRAN, 5.2, will most likely have evolved through several different versions at the launch of HyspIRI, and close collaboration with the MODTRAN developers will be maintained to keep up to date with the current versions. As for validation of previous versions, (Wan and Li 2008) have compared MODTRAN 4 simulations with clear-sky radiances from a well- calibrated, advanced Bomem TIR interferometer (MR100) and found accuracies to within 0.1 K for brightness temperature equivalent radiance values. It is expected that future versions will improve with spectral resolution and speed of execution.

Evaluation of atmospheric profile data accuracy at HyspIRI launch will be necessary to define uncertainty estimates for the atmospheric correction. Ideally, remote-sounding profiles will be used with observations close in time with HyspIRI. Current hyperspectral IR sounders (e.g., AIRS on Aqua, IASI on Metop) have accuracies of 1 K/km for temperature and 10% for relative humidity in the troposphere. These accuracies degrade over heterogeneous land surface due to uncertainties in surface emissivity; however, these accuracies are expected to improve over land in the next decade as improvements are made in characterization of the land surface emissivity.

It is expected that a beta version of the HyspIRI atmospheric correction production algorithm will be ready within approximately one year of launch, depending on the choice of atmospheric profile data, and made available at the Land Processes DAAC (LP DAAC). A simulation test dataset will be used to verify that the algorithm runs correctly at the LPDAAC, and subsequent changes and improvements to the beta version will be uploaded prior to launch.

The bulk of the atmospheric correction validation will involve testing and validation with JPL's Hyperspectral Thermal Emission Spectrometer (HyTES), an airborne sensor that has been developed specifically for support of the HyspIRI mission. The higher spatial (~30 m) and spectral resolution (256 bands from 7.5 to 12 μm) will help determine the optimal band placements for HyspIRI and also to assist with algorithm development. Expected launch of HyTES is sometime during 2012.

5.2 Post-launch

In-flight calibration and validation (calval) of TIR satellite data are essential for maintaining accuracy and precision of the instrument. The two most common types of calval methods are ground-based (in-situ) and aircraft-based. In ground-based calval, the surface radiance is measured by a ground-based radiometer, and the at-sensor radiance is forward modeled by estimating the atmospheric effects using atmospheric profiles with a radiative transfer model. The predicted at-sensor radiance is then compared to the observed radiance. For the aircraft-based method, data from an airborne sensor such as HyTES are acquired simultaneously with a satellite overpass, and a radiative transfer model is used to propagate this radiance to predict the at-satellite radiance. The aircraft measurements need to be well calibrated in order for this method to be successful. It is expected that calval of HyspIRI data will involve a combination of these two “vicarious” calibration methods. The validation of the atmospheric correction method is closely tied to the calibration of the instrument, since correction for atmospheric effects needs to be performed before at-surface radiance measurements can be compared to those at sensor.

We plan to use in-situ data from a variety of ground sites covering the majority of different land cover types defined in the International Geosphere-Biosphere Programme (IGBP). The sites will consist of water, vegetation (forest, grassland, savanna, and crops), and barren areas (Table 3).

Table 3: The core set of global validation sites according to IGBP class to be used for validation and calibration of the HyspIRI sensor.

IGBP Class		Sites
0	Water	Tahoe, Salton Sea, CA
1,2	Needle-leaf forest	Krasnoyarsk, Russia; Tharandt, Germany; Fairhope, Alaska;
3,4,5	Broad-leaf/mixed forest	Chang Baisan, China; Hainich, Germany; Hilo, Hawaii
6,7	Open/closed shrublands	Desert Rock, NV; Stovepipe Wells, CA
8,9,10	Savannas/Grasslands	Boulder, CO; Fort Peck, MT
12	Croplands	Bondville, IL, Penn State, PA; Sioux Falls, SD; Goodwin Creek, MS
16	Barren	Algodones dunes, CA; Great Sands, CO; White Sands, NM; Kelso Dunes, CA; Namib desert, Namibia; Kalahari, desert, Botswana

5.2.1 Water Targets

For water surfaces, we will use the Lake Tahoe, California/Nevada, automated validation site where measurements of skin temperature have been made every two minutes since 1999 and are used to validate the mid and thermal infrared data and products from ASTER and MODIS (Hook et al. 2007). Water targets are ideal for calval activities because they are thermally homogeneous and the emissivity is generally well known. Further advantages of Tahoe are that the lake is located at high altitude, which minimizes atmospheric correction errors, and it is large enough to validate sensors from pixel ranges of tens of meters to several kilometers. The typical range of temperatures at Tahoe is from 5°C to 25°C. More recently in 2008, an additional calval site at the Salton Sea was established. Salton Sea is a low altitude site with significantly warmer temperatures than Lake Tahoe (up to 35°C), and together they provide a wide range of different conditions.

5.2.2 *Vegetated Targets*

For vegetated surfaces (forest, grassland, savanna, and crops), we will use a combination of data from the Surface Radiation Budget Network (SURFRAD), FLUXNET, and NOAA-CRN sites. For SURFRAD, we will use a set of six sites established in 1993 for the continuous, long-term measurements of the surface radiation budget over the United States through the support of NOAA's Office of Global Programs (http://www.srrb.noaa.gov/surfrad/). The six sites (Bondville, IL; Boulder, CO; Fort Peck, MT; Goodwin Creek, MS; Penn State, PA; and Sioux Falls, SD) are situated in large, flat agricultural areas consisting of crops and grasslands and have previously been used to assess the MODIS and ASTER LST&E products with some success (Augustine et al. 2000; Wang and Liang 2009). From FLUXNET and the Carbon Europe Integrated Project (http://www.carboeurope.org/), we will include an additional four sites to cover the broadleaf and needleleaf forest biomes (e.g., Hainich and Tharandt, Germany; Chang Baisan, China; Krasnoyarsk, Russia) using data from the FLUXNET as well as data from the EOS Land Validation Core sites (http://landval.gsfc.nasa.gov/coresite_gen.html). Furthermore, the U.S. Climate Reference Network (USCRN) has been established to monitor present and future long-term climate data records (http://www.ncdc.noaa.gov/crn/). The network consists of 114 stations in the Continental USA and is monitored by NOAA’s National Climatic Data Center (NCDC). Initially we plan to use the Fairhope, Alaska, and Hilo, Hawaii, sites from this network.

6 Summary

HyspIRI is a NASA tier-2 mission recommended by the Earth Science Decadal Survey that will provide critical new capability for monitoring ecosystem response to natural and human-induced changes and identifying natural hazards such as volcanoes and wildfires. This document outlines the theory and methodology for generating the HyspIRI Level-2 thermal infrared (TIR) surface radiance product. The HyspIRI TIR instrument consists of a multispectral scanner with eight spectral bands operating between 4 and 12 µm, with a spatial scale of 60 m, revisit time of 5 days, and swath width of 600 km.

The surface radiance is primarily used as an input for the land surface temperature and emissivity algorithm. Atmospheric effects, including atmospheric emission, scattering, and absorption by the Earth's atmosphere, need to be removed from the measured radiance in order to isolate the land-leaving surface radiance contribution. The accuracy of the atmospheric correction is dependent upon accurate characterization of the atmospheric state with atmospheric profiles of temperature, water vapor, and other gas constituents (e.g., ozone). The profiles are typically input to a radiative transfer model such as MODTRAN for estimating atmospheric transmittance, path, and sky radiances. For HyspIRI, the surface radiance for each TIR band will be computed for all clear-sky pixels on a given scene using the best atmospheric profiles available at the time of launch (e.g., from NPOESS or model data such as NCEP) and using the most up-to-date version of MODTRAN radiative transfer model. Furthermore, a water vapor scaling (WVS) approach will be used to improve the accuracy of the atmospheric parameters in very humid conditions. This approach has proven to be successful in improving accuracy of the ASTER temperature and emissivity products.

Pre-launch validation and testing will involve determining the best combination of atmospheric profiles and radiative transfer model to remove atmospheric effects. Current plans are to use profiles from a future hyperspectral sounder such as CrIS on NPOESS, combined with the latest version of MODTRAN (currently v5.2). Further testing and sensitivity analysis will be performed with the Hyperspectral Thermal Emission Spectrometer (HyTES), an airborne sensor that has been developed specifically for support of the HyspIRI mission.

Post-launch validation will involve a combination of two "vicarious" calibration methods: ground-based and airborne measurements. In both methods, the predicted at-sensor radiance is estimated by forward modeling either the ground-based or aircraft-based radiance measurements. We plan to use *in situ* ground-based data from a variety of sites covering the majority of different land cover types defined in the International Geosphere-Biosphere Programme (IGBP). The sites will consist of water, vegetation (forest, grassland, savanna, and crops), and barren areas.

7 Future Work

7.1 Programming Considerations

The algorithm will be fairly simplistic with a small amount of code, but will call a radiative transfer (RT) model and multiple ancillary datasets, including atmospheric profiles and a DEM. With current computational capabilities, it is not feasible to run radiative transfer models on a pixel-by-pixel basis. Usually the RT model is run for several pixels covering the scene at a coarser resolution and then spatially interpolated to the pixel of choice using a higher resolution DEM. Several pre-launch tests will need to be run in order to find the most optimal balance between accuracy and computational time. Further tests will be needed to analyze the errors involved when temporally interpolating atmospheric profiles that are not coincident with HyspIRI observations. This can be tested by using numerical model profiles (e.g., NCEP) in six hourly intervals to assess the profile sensitivity errors to the HyspIRI observation time. We will also explore a look up table (LUT) approach where RT calculations will be run for a broad range of global atmospheric conditions and the atmospheric parameters will be estimated from the LUT given the input radiances for each band.

7.2 Water Vapor Scaling Coefficients

Once the HyspIRI TIR bands and spectral response functions are established, the water vapor scaling (WVS) coefficients will need to be determined using a global simulation model with input atmospheric parameters from either a numerical weather model or radiosonde data. Radiosonde databases such as the TIGR, SeeBor, and CLAR contain uniformly distributed global atmospheric soundings acquired both day and night in order to capture the full-scale natural atmospheric variability. A RT model such as MODTRAN is then used to estimate at-sensor and surface radiances for a wide range of different atmospheric conditions and surfaces, from which the coefficients are determined using a least-squares method.

7.3 Quality Assessment and Diagnostics

The surface radiance product will need to be assessed using a set of quality control (QC) flags. These QC flags will depend on the retrieval conditions, such as land or ocean surface, atmospheric water vapor content (dry, moist, very humid etc.), day or night, view angle, extreme conditions (very cold surfaces), high aerosol content, and temperature inversions. The magnitude of uncertainties related to each of these conditions will need to be assigned to the QC data plane and will be weighted depending on the sensitivity of each condition to the atmospheric correction. These weights will need to be determined using a sensitivity analysis and various other tests over different land cover types, for example.

8 Bibliography

Augustine, J.A., DeLuisi, J.J., & Long, C.N. (2000). SURFRAD - A national surface radiation budget network for atmospheric research. *Bulletin of the American Meteorological Society, 81,* (10), 2341-2357

Barton, I.J., Zavody, A.M., Obrien, D.M., Cutten, D.R., Saunders, R.W., & Llewellynjones, D.T. (1989). Theoretical Algorithms for Satellite-Derived Sea-Surface Temperatures. *Journal of Geophysical Research-Atmospheres, 94,* (D3), 3365-3375

Berk, A. (1989). MODTRAN: A moderate resolution model for LOWTRAN 7. *Spectral Sciences, Inc., Burlington, MA.*

Berk, A., Anderson, G.P., Acharya, P.K., Bernstein, L.S., Muratov, L., Lee, J., FOx, M., Adler-Golden, S.M., Chetwynd, J.H., Hoke, M.L., Lockwood, R.B., Gardner, J.A., Cooley, T.W., Borel, C.C., & Lewis, P.E. (2005). MODTRAN^{TM} 5, A Reformulated Atmospheric Band Model with Auxiliary Species and Practical Multiple Scattering Options: Update. S.S. Sylvia & P.E. Lewis (Eds.), *Algorithms and Technologies for Multispectral, Hyperspectral, and Ultraspectral Imagery XI*. Bellingham, WA: Proceedings of SPIE

Bosilovich, M.G., Chen, J.Y., Robertson, F.R., & Adler, R.F. (2008). Evaluation of global precipitation in reanalyses. *Journal of Applied Meteorology and Climatology, 47,* (9), 2279-2299

Coll, C., & Caselles, V. (1997). A split-window algorithm for land surface temperature from advanced very high resolution radiometer data: Validation and algorithm comparison. *Journal of Geophysical Research-Atmospheres, 102,* (D14), 16697-16713

Coll, C., Caselles, V., Valor, E., Niclos, R., Sanchez, J.M., Galve, J.M., & Mira, M. (2007). Temperature and emissivity separation from ASTER data for low spectral contrast surfaces. *Remote Sensing of Environment, 110,* (2), 162-175

Deschamps, P.Y., & Phulpin, T. (1980). Atmospheric Correction of Infrared Measurements of Sea-Surface Temperature Using Channels at 3.7, 11 and 12 Mu-M. *Boundary-Layer Meteorology, 18,* (2), 131-143

Francois, C., & Ottle, C. (1996). Atmospheric corrections in the thermal infrared: Global and water vapor dependent Split-Window algorithms - Applications to ATSR and AVHRR data. *IEEE Transactions on Geoscience and Remote Sensing, 34,* (2), 457-470

Galve, J.A., Coll, C., Caselles, V., & Valor, E. (2008). An atmospheric radiosounding database for generating land surface temperature algorithms. *IEEE Transactions on Geoscience and Remote Sensing, 46,* (5), 1547-1557

Gillespie, A., Rokugawa, S., Matsunaga, T., Cothern, J.S., Hook, S., & Kahle, A.B. (1998). A temperature and emissivity separation algorithm for Advanced Spaceborne Thermal Emission and Reflection Radiometer (ASTER) images. *IEEE Transactions on Geoscience and Remote Sensing, 36,* (4), 1113-1126

Gustafson, W.T., Gillespie, A.R., & Yamada, G.J. (2006). Revisions to the ASTER temperature/emissivity separation algorithm, *2nd International Symposium on Recent Advances in Quantitative Remote Sensing*. Torrent (Valencia), Spain

Hook, S.J., Gabell, A.R., Green, A.A., & Kealy, P.S. (1992). A Comparison of Techniques for Extracting Emissivity Information from Thermal Infrared Data for Geologic Studies. *Remote Sensing of Environment, 42,* (2), 123-135

Hulley, G.C., & Hook, S.J. (2009). The North American ASTER Land Surface Emissivity Database (NAALSED) Version 2.0. *Remote Sensing of Environment,* (113), 1967-1975

Justice, C., & Townshend, J. (2002). Special issue on the moderate resolution imaging spectroradiometer (MODIS): a new generation of land surface monitoring. *Remote Sensing of Environment, 83,* (1-2), 1-2

Kalnay, E., Kanamitsu, M., & Baker, W.E. (1990). Global Numerical Weather Prediction at the National-Meteorological-Center. *Bulletin of the American Meteorological Society, 71,* (10), 1410-1428

Kneizys, F.X., Abreu, L.W., Anderson, G.P., Chetwynd, J.H., Shettle, E.P., Berk, A., Bernstein, L.S., Robertson, D.C., Acharya, P.K., Rothman, L.A., Selby, J.E.A., Gallery, W.O., & Clough, S.A. (1996a). The MODTRAN 2/3 Report & LOWTRAN 7 Model, F19628-91-C-0132, *Phillips Lab*. Hanscom AFB, MA

Kneizys, F.X., Abreu, L.W., Anderson, G.P., Chetwynd, J.H., Shettle, E.P., Berk, A., Bernstein, L.S., Robertson, D.C., Acharya, P.K., Rothman, L.A., Selby, J.E.A., Gallery, W.O., & Clough, S.A. (1996b). The MODTRAN 2/3 Report & LOWTRAN 7 Model, F19628-91-C-0132. P. Lab. (Ed.). Hanscom AFB, MA

Li, Z.L., Becker, F., Stoll, M.P., & Wan, Z.M. (1999). Evaluation of six methods for extracting relative emissivity spectra from thermal infrared images. *Remote Sensing of Environment, 69,* (3), 197-214

NRC (2007). Earth Science and Applications from Space: National Imperatives for the Next Decade and Beyond, 2007. Committee on Earth Science and Applications from Space: A Community Assessment and Strategy for the Future*, National Research Council, National Academies Press. Referred to as the Decadal Survey or NRC 2007.*

Palluconi, F., Hoover, G., Alley, R.E., Nilsen, M.J., & Thompson, T. (1999). An atmospheric correction method for ASTER thermal radiometry over land, ASTER algorithm theoretical basis document (ATBD), Revision 3, Jet Propulsion Laboratory, Pasadena, CA, 1999

Prata, A.J. (1994). Land-Surface Temperatures Derived from the Advanced Very High-Resolution Radiometer and the Along-Track Scanning Radiometer .2. Experimental Results and Validation of Avhrr Algorithms. *Journal of Geophysical Research-Atmospheres, 99,* (D6), 13025-13058

Price, J.C. (1984). Land surface temperature measurements from the split window channels of the NOAA 7 Advanced Very High Resolution Radiometer. *Journal of Geophysical Research, 89,* (D5), 7231-7237

Seemann, S.W., Borbas, E.E., Knuteson, R.O., Stephenson, G.R., & Huang, H.L. (2008). Development of a global infrared land surface emissivity database for application to clear sky sounding retrievals from multispectral satellite radiance measurements. *Journal of Applied Meteorology and Climatology, 47,* (1), 108-123

Seemann, S.W., Li, J., Menzel, W.P., & Gumley, L.E. (2003). Operational retrieval of atmospheric temperature, moisture, and ozone from MODIS infrared radiances. *Journal of Applied Meteorology, 42,* (8), 1072-1091

Snyder, W.C., Wan, Z., Zhang, Y., & Feng, Y.Z. (1998). Classification-based emissivity for land surface temperature measurement from space. *International Journal of Remote Sensing, 19,* (14), 2753-2774

Susskind, J., Barnet, C.D., & Blaisdell, J.M. (2003). Retrieval of atmospheric and surface parameters from AIRS/AMSU/HSB data in the presence of clouds. *IEEE Transactions on Geoscience and Remote Sensing, 41,* (2), 390-409

Tonooka, H. (2005). Accurate atmospheric correction of ASTER thermal infrared imagery using the WVS method. *IEEE Transactions on Geoscience and Remote Sensing, 43,* (12), 2778-2792

Wan, Z., & Li, Z.L. (2008). Radiance-based validation of the V5 MODIS land-surface temperature product. *International Journal of Remote Sensing, 29,* (17-18), 5373-5395

Wan, Z.M., & Dozier, J. (1996). A generalized split-window algorithm for retrieving land-surface temperature from space. *IEEE Transactions on Geoscience and Remote Sensing, 34,* (4), 892-905

Wang, K.C., & Liang, S.L. (2009). Evaluation of ASTER and MODIS land surface temperature and emissivity products using long-term surface longwave radiation observations at SURFRAD sites. *Remote Sensing of Environment, 113,* (7), 1556-1565

Yu, Y., Privette, J.L., & Pinheiro, A.C. (2008). Evaluation of split-window land surface temperature algorithms for generating climate data records. *IEEE Transactions on Geoscience and Remote Sensing, 46,* (1), 179-192